

# Absolute Imaging of Low Conductivity Material Distributions Using Nonlinear Reconstruction Methods in Magnetic Induction Tomography

Bachir Dekdouk, Christos Ktistis, David W. Armitage, and Anthony J. Peyton\*

**Abstract**—Magnetic Induction Tomography (MIT) is a newly developing technique of electrical tomography that in principle is able to map the electrical conductivity distribution in the volume of objects. The image reconstruction problem in MIT is similar to electrical impedance tomography (EIT) in the sense that both seek to recover the conductivity map, but differ remarkably in the fact that data being inverted in MIT is derived from induction theory and related sources of noise are different. Progress in MIT image reconstruction is still limited, and so far mainly linear algorithms have been implemented. In difference imaging, step inversion was demonstrated for recovering perturbations within conductive media, but at the cost of producing qualitative images, whilst in absolute imaging, linear iterative algorithms have mostly been employed but mainly offering encouraging results for imaging isolated high conductive targets.

In this paper, we investigate the possibility of absolute imaging in 3D MIT of a target within conductive medium for low conductivity application ( $\sigma < 5 \text{ Sm}^{-1}$ ). For this class of problems, the MIT image reconstruction exhibits non-linearity and ill-posedness that cannot be treated with linear algorithms. We propose to implement for the first time in MIT two effective inversion methods known in non-linear optimization as Levenberg Marquardt (LMM) and Powell's Dog Leg (PDLM) methods. These methods employ damping and trust region techniques for controlling convergence and improving minimization of the objective function. An adaptive version of Gauss Newton is also presented (AGNM), which implements a damping mechanism to the regularization parameter. Here, the level of penalty is varied during the iterative process. As a comparison between the methods, different criteria are examined from image reconstructions using the LMM, PDLM and AGNM. For test examples, volumetric image reconstruction of a perturbation within homogeneous cylindrical background is considered. For inversion, an independent finite element FEM software package Maxwell by Ansys is employed to generate simulated data using a model of a 16 channel MIT system. Numerical results are employed to show different performance characteristics between the methods based on convergence, stability and sensitivity to the choice of the regularization parameter. To demonstrate the effect of scalability of absolute imaging in MIT for more realistic problems, a human head model with an internal anomaly is used to produce reconstructions for different finer resolutions. AGNM is adopted here and employs the Krylov subspace method to replace the computationally demanding direct inversion of the regularized Hessian.

## 1. INTRODUCTION

Magnetic Induction Tomography (MIT) is a nondestructive, soft field imaging technique for mapping the distribution of passive electromagnetic properties (e.g., electrical conductivity) of an object under

---

*Received 17 July 2015, Accepted 23 December 2015, Scheduled 11 January 2016*

\* Corresponding author: Anthony J. Peyton (a.peyton@manchester.ac.uk).

The authors are with the School of Electrical and Electronic Engineering, The University of Manchester, P. O. Box 88, M13 9PL, UK.

investigation [1, 2]. Unlike electrical impedance tomography (EIT), which requires electrodes to be attached to the surface of the object, MIT operates through an air gap using a set of excitation and detection coils. Hence, MIT appears to be attractive particularly for medical and some industrial process applications where the use of electrodes causes considerable distress to the patients or is practically inconvenient. MIT operates by passing a time varying sinusoidal current around an excitation coil which generates a primary magnetic field ( $\mathbf{B}_0$ ). When this field interacts with the electrical properties of the object, a perturbation secondary field ( $\Delta\mathbf{B}$ ) is produced, which is measured by an array of receiver coils in the form of induced voltages. When multiple excitations are used, a vector of measurement data is assembled and, with the help of an image reconstruction algorithm, the conductivity distribution inside the object can be estimated.

To date, the major progress reported in MIT image reconstruction mainly involved the application of linear algorithms including single step schemes such as linear back-projection [3, 4], Tikhonov regularization [5–10], truncated singular value decomposition (TSVD) [9], and iterative schemes like simultaneous iterative reconstruction technique (SIRT) [9], Landweber method [11] and the conjugate gradients least squares (CGLS) method [12]. Single step reconstruction methods are fast but they can only produce qualitative images. They have been implemented in difference imaging in space or time to resolve perturbations within conductive media. For problems involving reconstruction of isolated targets that are well separated within the scanning region, linear iterative routines were shown to produce successful qualitative imaging with improved resolution especially if such targets are highly conducting. However, if absolute reconstruction is sought for problems involving the resolution of inhomogeneities within a conductive region, then the application of such linear algorithms would be undesirable. This remark has been supported by an investigation made by Watson et al. [13] who suggested as a remedy to correct failed absolute reconstructions of a similar problem the necessity to investigate nonlinear methods. An initial investigation of absolute image reconstruction in MIT was then attempted by [14] using a nonlinear regularized Gauss Newton method.

In principle, the MIT image reconstruction involves the solution of an inverse problem that is ill-posed and nonlinear with respect to the conductivity distribution [14, 15]. The ill-posed problem renders the solution unstable and sensitive to measurement errors. As a consequence, the solution does not continuously depend on the observed data and small changes in the measurement data could often result in large reconstructed conductivity errors. The nonlinearity in the problem makes the measurement sensitivity map change markedly with conductivity variation in the background. For a suitable treatment of such a problem, nonlinear optimization can be applied while regularization can be used to reduce the ill-posedness of the problem.

In nonlinear optimization, a solution of the MIT inverse problem can be attained by minimizing a least squares objective function  $F$  given by:

$$F(\boldsymbol{\sigma}) = \frac{1}{2} \|\mathbf{F}(\boldsymbol{\sigma}) - \mathbf{D}\|^2 + \frac{1}{2} \lambda \|\mathbf{L}\boldsymbol{\sigma}\|^2 \quad (1)$$

where  $\boldsymbol{\sigma} \in \mathbb{R}^n$  is the conductivity vector,  $\mathbf{F}: \mathbb{R}^n \rightarrow \mathbb{R}^m$  the forward operator,  $\mathbf{D} \in \mathbb{R}^m$  the measured data, and  $(n, m)$  represent the number of image voxels and the number of measurements, respectively. The second least squares term is the Tikhonov penalty functional that is added to reduce the instability of the ill-posed problem by means of a regularization operator  $\mathbf{L} \in \mathbb{R}^{p \times n}$  with  $p = \text{rank}(\mathbf{L})$ , and a regularization parameter  $\lambda$ .

Starting with an initial guess  $\boldsymbol{\sigma}_0$ , the optimization (i.e., image reconstruction.) is carried out iteratively which produces a series of conductivity updates  $\{\boldsymbol{\sigma}_k | k = 1, 2, 3, \dots\}$  that desirably should converge towards a solution  $\boldsymbol{\sigma}^*$  that represents the global minimizer of the objective function  $F$ . These conductivity updates are obtained using the recurrence relation:

$$\boldsymbol{\sigma}_{k+1} = \boldsymbol{\sigma}_k + \alpha \mathbf{d} \quad (2)$$

where the vector  $\mathbf{d}$  is the “search direction”. Usually, this vector is computed with the constraint to produce the descending condition for the objective function given by:

$$F(\boldsymbol{\sigma}_{k+1}) < F(\boldsymbol{\sigma}_k) \quad (3)$$

and the scalar  $\alpha > 0$  is the “step length” which determines the size of the step along the direction  $\mathbf{d}$  that is able to provide an optimum decline in the objective function.

In order to calculate the search direction  $\mathbf{d}$  two widely known methods are used: the steepest descent direction and Newton's method. Using the former, the direction is calculated and the conductivity is updated as follows:

$$\boldsymbol{\sigma}_{k+1} = \boldsymbol{\sigma}_k + \alpha \mathbf{d}_{sd} = \boldsymbol{\sigma}_k - \alpha \nabla F(\boldsymbol{\sigma}_k) \quad (4)$$

Since only first order derivative information of the objective function is used in the calculation of the search direction, the method is often characterized by slow convergence. Nevertheless, the method can be effective in searching for the descent direction especially at the start of the iterative process. On the other hand, Newton's method requires the calculation of both the first and second order derivatives of the objective function in determining the search direction, which takes the form:

$$\boldsymbol{\sigma}_{k+1} = \boldsymbol{\sigma}_k + \mathbf{d}_N = \boldsymbol{\sigma}_k - \mathbf{H}^{-1} \nabla F(\boldsymbol{\sigma}_k) \quad (5)$$

where  $\mathbf{H} = \nabla^2 F(\boldsymbol{\sigma}_k)$  is the Hessian. As a consequence, Newton's method is relatively fast convergent, especially in the final stage of the iterative procedure. A quadratic convergence can be achieved if the Hessian  $\mathbf{H}$  is positive definite.

These two methods form the foundations of most nonlinear optimization methods applied for solving least squares problems. For instance, the Gauss Newton method (GNM) which has been widely applied in several areas including EIT and MIT is based on Newton's method. The equations that describe the regularized solution using GNM take the following form:

$$\begin{aligned} (\mathbf{J}_k^T \mathbf{J}_k + \lambda \mathbf{L}^T \mathbf{L}) \mathbf{d}_{rGN} &= -\mathbf{J}_k^T (\mathbf{F}(\boldsymbol{\sigma}_k) - \mathbf{D}) - \lambda \mathbf{L}^T \mathbf{L} \boldsymbol{\sigma}_k \\ \boldsymbol{\sigma}_{k+1} &= \boldsymbol{\sigma}_k + \mathbf{d}_{rGN} \end{aligned} \quad (6)$$

where  $\mathbf{J}_k \in \mathbb{R}^{m \times n}$  is the Jacobian matrix calculated in the  $k$ th iteration. As can be seen, GNM takes a full step length ( $\alpha = 1$ ) in computing the new conductivity vector. In [14, 15], Soleimani et al. employed this method to produce one of the first studies of absolute image reconstruction in MIT. In this paper, we propose to implement this method but with introducing a selection mechanism to the regularization factor. Usually the choice of this factor poses a difficulty to the user. In [14, 15], the regularization parameter has been fixed throughout the iterative process. A suggestion has been reflected in [15] to undertake studies to automate the choice of this parameter. Here, an adaptive process that is justified is applied to change this parameter during iterations with the intent to improve convergence. The process is automated and no time consuming traditional methods like the L-curve [16], which have been used in EIT [17], need to be applied.

In this paper, the interest is also directed to examine the performance of two other nonlinear optimization methods namely: the Levenberg Marquardt method (LMM) and Powell Dog Leg method (PDLM). In contrast to GNM, these methods are hybrid in the sense that they employ the steepest descent method and Newton's method using the application of damping and trust region techniques respectively. They have been implemented in different electrical tomography techniques including EIT [18, 19] ERT [20, 21] and ECT [22] and for both cases of pixel based and shape reconstruction. Here, these two methods will be studied for the first time for inversion of magnetic data obtained from an MIT array of sensors. The problem to be investigated is the performance of these methods for absolute reconstruction of a structural change within a conductive background within the scope of low conductivity applications. To the best of the author's knowledge, no MIT system has been produced with precision that satisfies the minimum requirements for experimental low conductivity absolute imaging. Therefore, data has been generated using an independent FEM software package, although it is believed that it is just a matter of time for such a precision in experimental hardware to be achieved. Comparison between the three methods using different criteria is performed using a simple low resolution test example. Later, scalability to relatively more realistic problems is considered and the effect of absolute MIT reconstruction with such problems is examined by using a realistic head model including a low contrast conductive feature with different higher resolutions. Adaptive Gauss Newton method (AGNM) is employed here for testing. In order to deal with the growing computational cost, the Krylov subspace method is implicitly implemented within the AGNM and comparisons are made to the standard form. Finally conclusions are made.

## 2. THEORY AND ALGORITHMS

### 2.1. Damping and Trust Region Techniques

Let us assume that the objective function  $F$  can be represented with a quadratic model  $M$  which approximates its behavior in the neighborhood of the current iterate  $(\boldsymbol{\sigma}_k)$  as:

$$M(\mathbf{d}) = F(\boldsymbol{\sigma}_k) + \mathbf{d}^T \nabla F(\boldsymbol{\sigma}_k) + \frac{1}{2} \mathbf{d}^T \mathbf{H} \mathbf{d} \quad (7)$$

When  $\mathbf{H}$  is exactly the Hessian  $\nabla^2 F(\boldsymbol{\sigma}_k)$ , the model  $M$  is identical to the Taylor series expansion of  $F(\boldsymbol{\sigma}_k + \mathbf{d})$  up to the second order term. The approximation error is then dominated by the third order term  $O(\|\mathbf{d}\|^3)$ . Hence, this infers that the model  $M$  is a good approximation to  $F(\boldsymbol{\sigma}_k + \mathbf{d})$  only when the step  $\mathbf{d}$  is small. Based on this model, the damping and trust region techniques can be introduced to compute the step  $\mathbf{d}$  that minimizes  $M$  but also adheres to additional constraints.

Using the damping technique, the step is determined as:

$$\mathbf{d} = \mathbf{d}_d = \mathop{\text{argmin}}_{\mathbf{d}} \left\{ M(\mathbf{d}) + \frac{1}{2} \gamma \mathbf{d}^T \mathbf{d} \right\} \quad (8)$$

where the scalar  $\gamma > 0$  is the damping parameter. As can be seen, the term  $(1/2) \gamma \mathbf{d}^T \mathbf{d} = (1/2) \gamma \|\mathbf{d}\|^2$  imposes a constraint on the step  $\mathbf{d}$ , and in this form is seen to penalise large magnitudes of the step.

In the trust region technique, a positive number  $\Delta > 0$  is defined as the radius of a sphere (i.e., a trust region) inside which the model is considered accurate (or equivalently trusted), and the step  $\mathbf{d}$  is computed as:

$$\mathbf{d} = \mathbf{d}_{tr} = \mathop{\text{argmin}}_{\mathbf{d}} \{ M(\mathbf{d}) \}, \quad \text{s.t. } \|\mathbf{d}\| \leq \Delta \quad (9)$$

After  $\mathbf{d}$  is evaluated, if the descending condition in (3) is met, the conductivity  $\boldsymbol{\sigma}_k$  is updated and  $\boldsymbol{\sigma}_{k+1}$  generated. Otherwise,  $\mathbf{d}$  is rejected. In this case, the damping parameter  $\gamma$  or the trust region radius  $\Delta$  needs to be modified and the step is recalculated with the hope that a descent direction will be achieved in the next iterate.

The process of updating  $\gamma$  or  $\Delta$  is controlled by the gain ratio ( $\rho$ ) which features the quality of the model  $M$  or equivalently determines how much the model  $M$  agrees with the objective function  $F$ . Once the step  $\mathbf{d}$  is calculated, the gain  $\rho$  is evaluated as follows:

$$\rho = \frac{F(\boldsymbol{\sigma}_k) - F(\boldsymbol{\sigma}_k + \mathbf{d})}{M(0) - M(\mathbf{d})} \quad (10)$$

where the denominator defines the predicted reduction in the objective function whereas the numerator evaluates the actual reduction in the  $M$  function value.

On the basis of the value of the gain ratio, we can discriminate between three cases:

- a) If  $\rho$  is negative, it means the numerator is negative since the denominator is always positive. This infers that the step  $\mathbf{d}$  was not descending and must be rejected. Hence, we must constrain the step to be smaller and repeat the iteration.
- b) If  $\rho$  is positive and smaller than 1, we may consider increasing the penalty on the magnitude of the step in the next iteration.
- c) If  $\rho$  is close to 1, the model function is a good approximation of the objective function, and we should take a larger step in the next iteration.

Both damped and trust region methods provide means to implement these conditions. In a damped method, a small value of the gain  $\rho$  indicates that we need to increase the parameter  $\gamma$  in the next iteration, which effectively reduce the step size; whereas a large value of  $\rho$  shows that our model  $M$  matches very well to the behavior of the objective function  $F$ , which suggests that  $\gamma$  can be decreased in the next iteration. In this paper we implement the Levenberg and Marquadt strategy following the form extracted from [23]:

Likewise, in the trust region method, the radius  $\Delta$  should be reduced to further constrain the step size if the value of  $\rho$  is small, or else,  $\Delta$  can be increased. The following trust region strategy [24] is adopted to control the step  $\mathbf{d}$  in this paper:

---


$$\begin{aligned}
&\text{if } \rho > 0 \\
&\quad \gamma = \gamma * \max(0.5, 1 - (2\rho - 1)^3); \quad \eta = 2; \\
&\text{else} \\
&\quad \gamma = \gamma * \eta; \quad \eta = \eta * 2
\end{aligned} \tag{11}$$


---

$$\begin{aligned}
&\text{if } \rho < 0.25 \\
&\quad \Delta = \Delta/2; \\
&\text{elseif } \rho > 0.75 \\
&\quad \Delta = \max(\Delta, 2 * \|\mathbf{d}\|); \\
&\text{else} \\
&\quad \Delta = \Delta;
\end{aligned} \tag{12}$$


---

## 2.2. Regularized Levenberg Marquardt Method

The LMM method is synthesized by introducing a damping factor to GNM. The relations for the Tikhonov regularized GNM described by Eq. (6) are modified and the step  $\mathbf{d}_{rLM}$  can thus be obtained by solving the following equation:

$$(\mathbf{J}_k^T \mathbf{J}_k + \gamma_k \mathbf{I} + \lambda \mathbf{L}^T \mathbf{L}) \mathbf{d}_{rLM} = -\mathbf{J}_k^T (\mathbf{F}(\boldsymbol{\sigma}_k) - \mathbf{D}) - \lambda \mathbf{L}^T \mathbf{L} \boldsymbol{\sigma}_k \tag{13}$$

and the conductivity iterate can be updated as:

$$\boldsymbol{\sigma}_{k+1} = \boldsymbol{\sigma}_k + \mathbf{d}_{rLM} \tag{14}$$

As  $\gamma_k$  is adjusted for each iteration, the term  $\gamma_k \mathbf{I}$  introduces the following effects:

- For  $\gamma_k$  sufficiently positive, the term  $\gamma_k \mathbf{I}$  can act as a regularisation operator, and may reflect prior information related to the identity matrix in the reconstructed image, depending on the magnitude of the elements in  $\gamma_k \mathbf{I}$  and  $\lambda \mathbf{L}^T \mathbf{L}$
- For very large value of  $\gamma_k$ , the effect of the term  $\gamma_k \mathbf{I}$  dominates that of  $(\mathbf{J}_k^T \mathbf{J}_k + \lambda \mathbf{L}^T \mathbf{L})$  so that:

$$\mathbf{d}_{LM} \approx -(1/\gamma) \mathbf{J}^T (\mathbf{F}(\boldsymbol{\sigma}) - \mathbf{D}) - \lambda \mathbf{L}^T \mathbf{L} \boldsymbol{\sigma} = -(1/\gamma) \mathbf{d}_{sd} \tag{15}$$

which approximates a step  $\alpha = 1/\gamma_k$  of the steepest descent method.

- When  $\gamma_k$  is too small compared to the elements in the coefficient matrix  $(\mathbf{J}_k^T \mathbf{J}_k + \lambda \mathbf{L}^T \mathbf{L})$ ,  $\mathbf{d}_{rLM}$  is effectively close to the Gauss Newton step. Therefore, the LMM can be regarded as a hybrid method in which two different methods are employed in a single optimization problem.

In the LMM iterative process, we usually start with a large value of  $\gamma_k$ . The latter is then reduced whenever the objective function records a minimization level compatible with that of the model  $M$ . This is intended to push the algorithm towards the Gauss Newton method as we approach the final stage of the iteration. When the iterate solution attains the minimizer  $\boldsymbol{\sigma}^*$ , the LM method switches to the steepest descent method whereby  $\gamma_k$  is increased in order to reduce the magnitude of the step  $\mathbf{d}_{rLM}$ . This is meant to prevent the algorithm from a possible unwanted divergence away from the minimizer  $\boldsymbol{\sigma}^*$ .

The damping parameter  $\gamma_k$  is updated as illustrated in Section 2.1 based on the value of the gain ratio  $\rho$ . It should be noted that when calculating the ratio ( $\rho$ ), the step  $\mathbf{d}_{rLM}$  in the denominator of  $\rho$  is replaced by  $(\delta \boldsymbol{\sigma}_k = \boldsymbol{\sigma}_{k+1} - \boldsymbol{\sigma}_k)$ . This is because when  $\boldsymbol{\sigma}_{k+1}$  is updated with the step  $\mathbf{d}_{LM}$ , non negativity constraining is applied to constrain any generated negative conductivity elements within  $\boldsymbol{\sigma}_{k+1}$  to a small positive value near zero ( $v = 1 \times 10^{-4}$ ), which alters the step to be  $\delta \boldsymbol{\sigma}_k$ . This procedure is applied to all algorithms presented in this paper.

In order to terminate the iterations, two stopping criteria are used: a) When a maximum number of iterations ( $k_{\max}$ ) is reached. b) When the inequality condition  $\|\boldsymbol{\sigma}_{k+1} - \boldsymbol{\sigma}_k\| < \varepsilon(\|\boldsymbol{\sigma}_k + \varepsilon\|)$  is met, where  $\varepsilon$  is a small positive number specified by the user. The LMM algorithm is depicted in a pseudo form in Figure 1.

**Problem:**

$\operatorname{argmin}_{\sigma \in \mathbb{R}^n} \{ F(\sigma) \}; F(\sigma) = \frac{1}{2} \|\mathbf{F}(\sigma) - \mathbf{D}\|^2 + \frac{1}{2} \lambda \|\mathbf{L}\sigma\|^2$

Evaluate the objective function:

$$F(\sigma_0) = \frac{1}{2} \|\mathbf{F}(\sigma_0) - \mathbf{D}\|^2 + \frac{1}{2} \lambda_0 \|\mathbf{L}\sigma_0\|^2;$$

Compute the gradient:  $\mathbf{g} = \mathbf{J}(\sigma_0)^T (\mathbf{F}(\sigma_0) - \mathbf{D}) + \lambda_0 \mathbf{L}^T \mathbf{L}\sigma_0$ ;

Calculate:  $\mathbf{A} = \mathbf{J}(\sigma_0)^T \mathbf{J}(\sigma_0)$ ;

Set  $\gamma = 10^{-3} \times \lambda_0$ ;  $k = 0$ ; set  $k_{\max}$ ;  $exit = \text{false}$ ;

**while**  $k < k_{\max}$  and  $exit \neq \text{true}$

Compute the Hessian:  $\mathbf{H}_{rLM} = \mathbf{A} + \gamma \mathbf{I} + \lambda \mathbf{L}^T \mathbf{L}$ ;

Calculate the step:  $\mathbf{d}_{rLM} = -\mathbf{H}_{rLM}^{-1} \mathbf{g}$ ;

Update the conductivity map:  $\sigma_{New} = \sigma_k + \mathbf{d}_{rLM}$ ;

Constrain the conductivity map:

$$\begin{cases} i = 1:n | (\sigma_{New}(i) < 0) = \nu \approx 0 \\ i = 1:n | (\sigma_{New}(i) > \sigma_{\max}) = \sigma_{\max} \end{cases}$$

**if**  $\|\sigma_{New} - \sigma_k\| < \varepsilon (\|\sigma_k\| + \varepsilon)$

$exit = \text{true}$ ;

**else**

Evaluate the objective function:

$$F(\sigma_{New}) = \frac{1}{2} \|\mathbf{F}(\sigma_{New}) - \mathbf{D}\|^2 + \frac{1}{2} \lambda \|\mathbf{L}\sigma_{New}\|^2;$$

Calculate the gain ratio:

$$\rho = (F(\sigma_k) - F(\sigma_{New})) / (M(0) - M(\sigma_{New} - \sigma_k));$$

**if**  $\rho > 0$

$\sigma_{k+1} = \sigma_{New}$ ;

$\mathbf{g} = \mathbf{J}(\sigma_{k+1})^T (\mathbf{F}(\sigma_{k+1}) - \mathbf{D}) + \lambda \mathbf{L}^T \mathbf{L}\sigma_{k+1}$ ;

$\mathbf{A} = \mathbf{J}(\sigma_{k+1})^T \mathbf{J}(\sigma_{k+1})$ ;

$\gamma = \gamma * \max(0.5, 1 - (2\rho - 1)^3)$ ;  $\eta = 2$ ;

**else**

$\gamma = \gamma * \eta$ ;

$\eta = \eta * 2$ ;

**if**  $\eta > 32$   $exit = \text{true}$ ; **end**

**end**

$k = k + 1$ ;

**end**

**Figure 1.** Regularized Levenberg Marquardt Method.

**Problem:**

$\operatorname{argmin}_{\sigma \in \mathbb{R}^n} \{ F(\sigma) \}; F(\sigma) = \frac{1}{2} \|\mathbf{F}(\sigma) - \mathbf{D}\|^2 + \frac{1}{2} \lambda \|\mathbf{L}\sigma\|^2$

Evaluate the objective function:

$$F(\sigma_0) = \frac{1}{2} \|\mathbf{F}(\sigma_0) - \mathbf{D}\|^2 + \frac{1}{2} \lambda_0 \|\mathbf{L}\sigma_0\|^2;$$

Compute the gradient:  $\mathbf{g} = \mathbf{J}(\sigma_0)^T (\mathbf{F}(\sigma_0) - \mathbf{D}) + \lambda_0 \mathbf{L}^T \mathbf{L}\sigma_0$ ;

Calculate:  $\mathbf{A} = \mathbf{J}(\sigma_0)^T \mathbf{J}(\sigma_0)$ ;

Set  $\Delta = \Delta_0$

Compute the Hessian:  $\mathbf{H}_{rGN} = \mathbf{A} + \lambda \mathbf{L}^T \mathbf{L}$ ;

Calculate the step:  $\mathbf{d}_{rGN} = -\mathbf{H}_{rGN}^{-1} \mathbf{g}$ ;

Compute  $\alpha$  by (17)

$k = 0$ ; set  $k_{\max}$ ;  $exit = \text{false}$ ;  $\eta = 0$ ;

**while**  $k < k_{\max}$  and  $exit \neq \text{true}$

Compute  $\mathbf{d}_{rPDL}$  by (18)

Update the conductivity map:  $\sigma_{New} = \sigma_k + \mathbf{d}_{rPDL}$ ;

Constrain the conductivity map:

$$\begin{cases} i = 1:n | (\sigma_{New}(i) < 0) = \nu \approx 0 \\ i = 1:n | (\sigma_{New}(i) > \sigma_{\max}) = \sigma_{\max} \end{cases}$$

**if**  $\|\sigma_{New} - \sigma_k\| < \varepsilon (\|\sigma_k\| + \varepsilon)$

$exit = \text{true}$ ;

**else**

Evaluate the objective function:

$$F(\sigma_{New}) = \frac{1}{2} \|\mathbf{F}(\sigma_{New}) - \mathbf{D}\|^2 + \frac{1}{2} \lambda \|\mathbf{L}\sigma_{New}\|^2;$$

Calculate the gain ratio:

$$\rho = (F(\sigma_k) - F(\sigma_{New})) / (M(0) - M(\sigma_{New} - \sigma_k));$$

**if**  $\rho < 0.25$

$\Delta = \Delta / 2$ ;

**elseif**  $\rho > 0.75$

$\Delta = \max(\Delta, 2 * \|\mathbf{d}_{rPDL}\|)$ ;

**end**

**if**  $\rho > 0$

$\sigma_{k+1} = \sigma_{New}$ ;

$\mathbf{g} = \mathbf{J}(\sigma_{k+1})^T (\mathbf{F}(\sigma_{k+1}) - \mathbf{D}) + \lambda \mathbf{L}^T \mathbf{L}\sigma_{k+1}$ ;

$\mathbf{H}_{rGN} = \mathbf{J}(\sigma_{k+1})^T \mathbf{J}(\sigma_{k+1}) + \lambda \mathbf{L}^T \mathbf{L}$ ;

Compute  $\alpha$  by (17)

**else**

$\eta = \eta + 1$ ;

**if**  $\eta > 5$   $exit = \text{true}$ ; **end**

**end**;  $k = k + 1$ ;  $\eta = 0$ ;

**end**

**Figure 2.** Trust region Powell Dog Leg Method.

### 2.3. Trust Region Powell's Dog Leg Method

The Powell's Dog Leg method (PDL) employs the trust region strategy described in Section 2.1. Using this method, the step length and direction are controlled explicitly via the radius of the trust region. Like the LM method, the PDL method works in combination between the Gauss Newton method and the steepest descent method. The trust region and the LM methods are closely related. In fact, it has been shown in [25] that for a positive damping parameter ( $\gamma > 0$ ), the computed LM step  $\mathbf{d}_{rLM}$

satisfies:

$$\mathbf{d}_{rLM} = \underset{\mathbf{d}}{\operatorname{argmin}} \left\{ \underbrace{F(\boldsymbol{\sigma}) + \mathbf{d}^T \nabla F(\boldsymbol{\sigma}) + \frac{1}{2} \mathbf{d}^T \mathbf{H} \mathbf{d}}_{M(\mathbf{d})} \right\}, \quad s.t. \|\mathbf{d}\| \leq \|\mathbf{d}_{rLM}\| \quad (16)$$

Given the current iterate  $\boldsymbol{\sigma}_k$ , the step  $\mathbf{d}$  needed to obtain the next iterate  $\boldsymbol{\sigma}_{k+1}$  can be calculated by the regularized Gauss Newton method using the system of Equation (6). Alternatively, it can also be evaluated via the steepest descent method using (4), where the step factor  $\alpha$  can be computed via the relation given by:

$$\alpha = -\frac{\mathbf{d}_{sd}^T \nabla F(\boldsymbol{\sigma}_k)}{\nabla F(\boldsymbol{\sigma}_k)^T \mathbf{H}_{rGN} \nabla F(\boldsymbol{\sigma}_k)} = \frac{\|\nabla F(\boldsymbol{\sigma}_k)\|^2}{\nabla F(\boldsymbol{\sigma}_k)^T \mathbf{H}_{rGN} \nabla F(\boldsymbol{\sigma}_k)} \quad (17)$$

By having two candidates for computing the next iterate vector  $\boldsymbol{\sigma}_{k+1}$ , namely:  $\mathbf{a} = \alpha \mathbf{d}_{sd}$ , and  $\mathbf{b} = \mathbf{d}_{rGN}$ , Powell proposed the following strategy for calculating the trust region step  $\mathbf{d}_{trPDL}$ , when the trust region has a radius  $\Delta$ :

---


$$\begin{aligned} &\text{if } \|\mathbf{d}_{rGN}\| \leq \Delta \\ &\quad \mathbf{d}_{trPDL} = \mathbf{d}_{rGN}; \\ &\text{elseif } \|\alpha \mathbf{d}_{sd}\| \geq \Delta \\ &\quad \mathbf{d}_{trPDL} = (\Delta / \|\mathbf{d}_{sd}\|) * \mathbf{d}_{sd}; \\ &\text{else} \\ &\quad \mathbf{d}_{trPDL} = \alpha \mathbf{d}_{sd} + \zeta (\mathbf{d}_{rGN} - \alpha \mathbf{d}_{sd}); \text{ s.t. } \|\mathbf{d}_{trPDL}\| = \Delta; \end{aligned} \quad (18)$$


---

With  $\mathbf{a}$  and  $\mathbf{b}$  defined as above, and  $\mathbf{c} = \mathbf{a}^T (\mathbf{b} - \mathbf{a})$ , the positive scalar  $\zeta > 0$  can be determined by taking the positive root of the quadratic equation in  $\zeta$  defined by:

$$\varphi(\zeta) = \|\mathbf{a} + \zeta (\mathbf{b} - \mathbf{a})\|^2 - \Delta^2 = \|\mathbf{b} - \mathbf{a}\|^2 \zeta^2 + 2\mathbf{c}\zeta + \|\mathbf{a}\|^2 - \Delta^2 \quad (19)$$

As in the LM method, the gain ratio  $\rho$  is used in the same fashion to control the size of the trust region radius  $\Delta$ . The same stopping criteria as for the LM method are applied here due the similarity in the characteristics of both methods. The pseudo form of the algorithm is presented in Figure 2.

#### 2.4. Adaptive Gauss Newton Method

In the LMM and PDLM, the amount of regularization imposed by the Tikhonov operator ( $\mathbf{R} = \mathbf{L}^T \mathbf{L}$ ) on the elements of the coefficient matrix ( $\mathbf{J}^T \mathbf{J}$ ) and the residual ( $\mathbf{F}(\boldsymbol{\sigma}) - \mathbf{D}$ ) is held unchanged through the iterations with a fixed regularization parameter. However, the ill-conditioning of the Jacobian and residual error varies from one iteration to another. This suggests that adapting the amount of regularization can be another option to optimize the convergence. It is well known that increasing the regularization weight will raise the filtering level of high frequency components in the data and strengthen the assumed prior information on the inverse solution, whereas decreasing such regularization will reduce the filtering barrier and facilitate the reconstruction of high frequency components in the image. While the large features of the image are usually recovered in the first few iterations, regularization weight can therefore be changed to aid some of the high resolution features in the image to be reconstructed as the iterative procedure progresses.

In this paper we present a modified version of GNM with the regularisation parameter involved in an adaptive process to implement this principle. The step  $\mathbf{d}_{dGN}$  is calculated using the following equations:

$$(\mathbf{J}_k^T \mathbf{J}_k + \lambda_k \mathbf{L}^T \mathbf{L}) \mathbf{d}_{dGN} = -\mathbf{J}_k^T (\mathbf{F}(\boldsymbol{\sigma}_k) - \mathbf{D}) - \lambda_k \mathbf{L}^T \mathbf{L} \boldsymbol{\sigma}_k \quad (20)$$

$$\boldsymbol{\sigma}_{k+1} = \boldsymbol{\sigma}_k + \mathbf{d}_{dGN} \quad (21)$$

where the regularisation parameter  $\lambda_k$  is now adaptable and selected in an identical manner to the damping parameter  $\gamma_k$  in the LM method. The following traits can be extracted from this reconstruction algorithm:

- a) The algorithm is not sensitive to the initial choice of the regularisation parameter  $\lambda_k$  compared to the LM or the PDL methods. The image reconstruction can start with a large  $\lambda_k$  that produces a sufficiently smooth image, which is then gradually decreased to allow rapid changes in the image to be reconstructed.
- b) In case of poor accord between the reduction in the model  $M$  and the objective function  $F$ , the hyper-parameter  $\lambda_k$  is increased with the aim of enhancing the regularisation, hoping stability will be restored and the step be improved in the next iteration.

It is worth noting that this is not the first time an automated procedure for selecting the regularisation parameter was investigated. In [26], a flexible Arnoldi Tikhonov method was presented for sparse image reconstruction, where a procedure for adapting the regularisation parameter was demonstrated within the solution of a linear least squares problem. However, this procedure differs from the approach proposed in this paper, in the sense that a discrepancy principle was used in [26] with a formulation to recursively change  $\lambda_k$  until the data residual fall just above the noise level that is assumed to be known in the data. Once this balance is achieved, no more changes in  $\lambda_k$  are observed, which prompted the authors to consider a restarting procedure to be implemented within the algorithm.

The algorithm illustrated in this paper is shown in Figure 3.

## 2.5. Forward Model and Sensitivity Matrix

The forward problem in MIT is a nonlinear eddy current problem which is described by Maxwell's equations and the associated constitutive laws of electromagnetism. This problem can be solved using the finite element method [27, 28], finite difference method [29] or boundary element method [30]. The latter technique is known to be fast compared to FEM or FDM, since it only discretizes the boundaries of the background and the internal features, and can be found appropriate for a limited range of problems including shape reconstruction of objects with homogeneous material distribution, whereas FEM or FDM are more general however they require meshing the entire problem leading to larger number of unknowns [20]. In this paper, we propose to use a voxel-based custom forward solver that we have developed in [29]. This solver has been implemented using the impedance method based on the finite difference method. Using this method, the object is discretized into a Cartesian mesh of regular cubic voxels where each voxel is assumed to have a uniform conductivity. Thus, the object can be visualized as a network of interconnected electrical impedances for which the eddy currents are solved. To make nonlinear reconstruction feasible, the employed solver adopted a weakly coupled field approximation that has been validated rigorously in [31]. This approximation fits very well imaging applications involving materials with low conductivity distributions which are targeted in this paper. Hence, with this solver, a significant gain in the computational cost is achieved.

The inversion also requires an efficient calculation of the sensitivity matrix ( $\mathbf{J} = d\mathbf{F}/d\boldsymbol{\sigma}$ ) which maps changes in the conductivity distribution  $d\boldsymbol{\sigma}$  into changes in the received voltages  $d\mathbf{V}$ . We employ the  $(\mathbf{E} \cdot \mathbf{E})$  formulation which is based on an extension of the Gezelowitz theorem to the general electromagnetic case [32]. This formulation is derived assuming conductivity changes are small, and hence it can be satisfactorily applied for low contrast applications which form the scope of this paper. In addition, the evaluations of this matrix is relatively inexpensive compared to other possible methods since it only requires the electric fields to be calculated in the volume of the target, which can be obtained from the forward problem solutions.

## 3. SIMULATION SETUP AND TEST PROCEDURE

The MIT system used in this computational experiment is depicted in Figure 4(a). The modelling of the system has been performed in two FE software packages, namely COMSOL by Multiphysics and Maxwell by Ansys. The system components include a cylindrical shield for electromagnetic insulation with radius of 175 mm, height of 250 mm, and a circular coil array which consists of 16 excitation coils and 16 receiver coils (diameter 50 mm) arranged in two concentric circles at radii of 141.5 mm and 131.5 mm surrounding the target. The excitation coils are sequentially driven with a time varying sinusoidal unit current for simplicity, and induced voltages are obtained from the receiver coils. The excitation frequency is set to 10 MHz. The measurement data is simulated using Maxwell for the phantom placed

**Problem:**

$\operatorname{argmin}_{\sigma \in R^n} \{ F(\sigma) \}; F(\sigma) = \frac{1}{2} \| \mathbf{F}(\sigma) - \mathbf{D} \|^2 + \frac{1}{2} \lambda \| \mathbf{L}\sigma \|^2$

Evaluate the objective function:

$$F(\sigma_0) = \frac{1}{2} \| \mathbf{F}(\sigma_0) - \mathbf{D} \|^2 + \frac{1}{2} \lambda_0 \| \mathbf{L}\sigma_0 \|^2;$$

Compute the gradient:  $\mathbf{g} = \mathbf{J}(\sigma_0)^T (\mathbf{F}(\sigma_0) - \mathbf{D}) + \lambda_0 \mathbf{L}^T \mathbf{L}\sigma_0$ ;

Calculate:  $\mathbf{A} = \mathbf{J}(\sigma_0)^T \mathbf{J}(\sigma_0)$ ;

Set  $\lambda = \lambda_0$ ;  $k = 0$ ; set  $k_{\max}$ ;  $exit = \text{false}$ ;

**while**  $k < k_{\max}$  and  $exit \neq \text{true}$

    Compute the Hessian:  $\mathbf{H}_{dGN} = \mathbf{A} + \lambda \mathbf{L}^T \mathbf{L}$ ;

    Calculate the step:  $\mathbf{d}_{dGN} = -\mathbf{H}_{dGN}^{-1} \mathbf{g}$ ;

    Update the conductivity map:  $\sigma_{New} = \sigma_k + \mathbf{d}_{dGN}$ ;

    Constrain the conductivity map:

$$\begin{cases} i = 1:n | (\sigma_{New}(i) < 0) = \nu \approx 0 \\ i = 1:n | (\sigma_{New}(i) > \sigma_{\max}) = \sigma_{\max} \end{cases}$$

    Evaluate the objective function:

$$F(\sigma_{New}) = \frac{1}{2} \| \mathbf{F}(\sigma_{New}) - \mathbf{D} \|^2 + \frac{1}{2} \lambda \| \mathbf{L}\sigma_{New} \|^2;$$

    Calculate the gain ratio:

$$\rho = (F(\sigma_k) - F(\sigma_{New})) / (M(0) - M(\sigma_{New} - \sigma_k))$$

    ;

**if**  $\rho > 0$

$\sigma_{k+1} = \sigma_{New}$ ;

$\lambda = \lambda * \max(0.5, 1 - (2\rho - 1)^3)$ ;  $\eta = 2$ ;

$\mathbf{g} = \mathbf{J}(\sigma_{k+1})^T (\mathbf{F}(\sigma_{k+1}) - \mathbf{D}) + \lambda \mathbf{L}^T \mathbf{L}\sigma_{k+1}$ ;

$\mathbf{A} = \mathbf{J}(\sigma_{k+1})^T \mathbf{J}(\sigma_{k+1})$ ;

**else**

$\lambda = \lambda * \eta$ ;

$\eta = \eta * 2$ ;

**if**  $\eta > 32$   $exit = \text{true}$ ; **end**

**end**

$k = k + 1$ ;

**end**

**Figure 3.** Adaptive Gauss Newton Method.

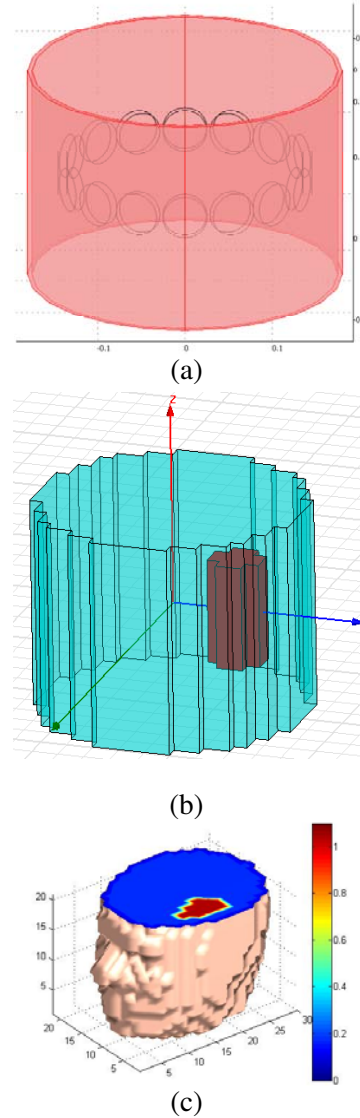


**Figure 4.** Simulated models of (a) the MIT coil array, (b) simple example with a perturbation and (c) head model with an anomaly.

inside the MIT system and modeled with the true conductivity distribution. The forward problem is solved using the custom eddy current solver. The latter requires a computation of the primary magnetic vector potential  $\mathbf{A}_0$  in the empty space occupied by the phantom, which is obtained from COMSOL. In order to increase the number of independent measurements, 9 planes of projections were taken by displacing the MIT system comprising the coil array and the screen along the  $z$  direction in steps of 20 mm over the interval  $z \in [-80, 80]$  mm. The multiple measurement planes also enhance sensitivity and provide more eddy current information throughout the volume of the phantom which will help the 3D image reconstruction. In total, 2034 independent simulated measurement data were collected.

For scanning, a simulated simple phantom crudely approximating a human head with a lesion is considered (Figure 4(b)). The phantom consists of a background cylinder (diameter: 20 cm; height: 16 cm) centered at the origin, and a cylindrical perturbation (diameter: 4 cm; height: 8 cm) centered at (0, 5, 0) cm in the  $(x, y, z)$  co-ordinate space. The phantom has been discretised into 5056 cubic voxels of  $10 \times 10 \times 10 \text{ mm}^3$  resolution, of which 96 elements were allocated to the perturbation. Notice

the blocky form of the edges of the background and the perturbation, which do not conform to the smooth cylindrical boundaries of real objects. This is a problem from which this type of regular cubic discretization suffers, especially at low resolutions. In this study we are however interested in investigating the performance of the optimization methods using a phantom of a given structure and the treatment of the edges is not the immediate topic of investigation here. The background and the perturbation were assigned conductivities of  $0.16 \text{ Sm}^{-1}$  and,  $1.1 \text{ Sm}^{-1}$  respectively corresponding to reported values for biological tissues of white matter and blood at 10 MHz excitation frequency [33].

For image reconstruction, the iterative optimisation algorithms require an initial guess  $\sigma_0$ . This is computed with a single step by Tikhonov method as:

$$\sigma_0 = -(\mathbf{J}_0^T \mathbf{J}_0 + \lambda_0 \mathbf{L}^T \mathbf{L})^{-1} \mathbf{J}_0^T \mathbf{D} \quad (22)$$

where  $\mathbf{L}$  is a smoothing 2nd order derivative operator referred to as the Neighbouring matrix [15], and the regularisation parameter  $\lambda_0$  was calculated based on the order of magnitude of the elements in  $[\mathbf{J}_0^T \mathbf{J}_0]$  as in [34]. The Jacobian  $\mathbf{J}_0$  is computed for a homogenous conductivity distribution (e.g,  $\sigma = 1 \text{ Sm}^{-1}$ ) in the phantom. Hence, this gives:

$$\lambda_0 = \tau * \max_{i=1, \dots, n} \left( [\mathbf{J}_0^T \mathbf{J}_0]_{(i,i)} \right) \quad (23)$$

Here,  $\tau$  is chosen by the user, and depends on the severity of noise expected in the data. In this paper, data was generated from a FEM model with a mesh different from that employed in solving the inverse problem; the FEM model exploits a tetrahedral mesh whereas the algorithm uses a Cartesian mesh, as explained above. Compared to a noise free dataset, the percentage relative rms value of the noise present in the measurement dataset was evaluated to be 2.36%. Thus, we found that  $\tau = 1 \times 10^2$  is a good choice in this example. For the selection of regularisation parameter in the iterative reconstruction schemes, AGNM starts with  $\lambda_1 = \lambda_0$ , and for the LMM and PDLM, the image reconstruction was repeated for three values of  $\lambda$ :  $[10^{-1}, 10^{-2}, 10^{-3}] \times \lambda_0$ . Another possibility could have been to use a parameter selection method such as the L-curve, or the discrepancy theorem to choose  $\lambda$ .

In a following test procedure, a further step is taken to examine the performance of absolute imaging in MIT using more realistic models with finer resolutions. This is due to the fact that in many MIT applications particularly in the medical field, the inverse problem may need to be solved with large number of degrees of freedom. Hence, it is important to examine the scalability to different resolutions with the proposed optimisation methods. Among these algorithms, AGNM is employed for this examination. As known, AGNM solution is achieved through iterative solutions of linearized steps involving direct inversion of regularised Hessian. For a large scale problem, the latter results in an oversized matrix for which direct inversion is computationally demanding. In order to deal with this problem, a linear iterative Conjugate Gradient method is applied to estimate the linearised step  $\mathbf{d}_{dGN}$  used to update the iterate  $\sigma_k$  within the AGNM algorithm by replacing a direct inverse equation described in Eq. (20) by the following iterative algorithm:

---

```

r0 = -gk - Hkd0; n = 0
while ||rn||/||r0|| > tol do
  n = n + 1
  z = Θ\r
  if n = 1
    p = z
  else
     $\beta_n = (\mathbf{r}_{n-1}^T \mathbf{z}_{n-1}) / (\mathbf{r}_{n-2}^T \mathbf{z}_{n-2})$ 
    pn = zn-1 +  $\beta_n$ pn-1
  end
   $\alpha_n = (\mathbf{r}_{n-1}^T \mathbf{z}_{n-1}) / (\mathbf{p}_n^T \mathbf{H}_k \mathbf{p}_n)$ 
  dn = dn-1 +  $\alpha_n$ pn
  rn = rn-1 -  $\alpha_n$ Hkpn
end

```

---

This insertion of linear CG method into the nonlinear Gauss Newton algorithm to produce an estimate for direct inversion of the Hessian still employs 2nd order derivative information of the objective function. A proposition of such implementation has been presented in Horesh [35] and Polydorides [36]. Notice that the algorithm in Eq. (24) incorporates a preconditioner  $\Theta$  which is used to optimise the CG convergence and is described by:

$$\Theta = \text{diag} \left( \sum_{j=i} \mathbf{J}_{ji} + \lambda_k \right) \quad (25)$$

For testing, the following problems with different numbers of unknown conductivity elements (DoFs) are considered as follows:

- a) Cylindrical background and an inclusion comprising 5056 DoFs as described above.
- b) Head model (H1) (White matter and large stroke) comprising 9012 DoFs.
- c) Head model (H2) (White matter and large stroke) comprising 30405 DoFs.

The two employed head models were obtained from an FE head model that was created by Holder et al. from University College London who applied 53,336 FEs meshing 7 compositional biological tissues. Since the scale (size) of the problem is the main focus of this investigation, two tissues were considered for simplicity namely: white matter and an anomaly (blood clot) representing a stroke as shown in Figure 4(c). Similarly, 2304 simulated measured data was collected, but without noise being added, and absolute images for the three conductivity models were generated. In order to examine the computational benefits of this method, the same image reconstruction was carried out with the direct inversion based AGNM method. Reconstruction results from the AGNM employing CG method as a subset routine were termed AGNM-CG. Comparisons were made taking into account computational costs and image reconstruction quality.

## 4. RESULTS AND DISCUSSION

In order to test the performance of the algorithms in solving the MIT inverse problem for absolute imaging of low conductivity profiles, the results of image reconstruction have been analysed using the example (Figure 4(b)) and compared based on the following criteria:

- a) Convergence of the objective function  $F$ .
- b) Convergence of the solution (reconstructed conductivity) error  $\|\sigma_k - \sigma_{true}\|/\|\sigma_{true}\|$ .
- c) Stability of the algorithm.
- d) Robustness of the selected stopping criteria.
- e) Sensitivity to the choice of the regularisation parameter.

### 4.1. Convergence of the Objective Function

The LMM and PDLM algorithms exhibited different levels of convergence for different values  $\lambda$ . This is shown in Figure 5 and Figure 8. This infers that the algorithms are sensitive to the choice of the regularisation parameter  $\lambda$ . The optimum minimization of the objective function has been achieved for the case when  $\lambda = 1 \times 10^{-3}$ . On the other hand, AGNM (Figure 10(a)) produced a better convergence compared to its counterparts, LMM and PDLM.

### 4.2. Convergence of the Solution Error

While the convergence error of the objective function is an available criterion to assess how efficient nonlinear optimization methods are in minimizing the least squares problem  $F$ , the conductivity solution error is the major criterion with the ultimate answer to which optimization method is robust to produce a good local minimizer  $\sigma^*$  closer to the true distribution  $\sigma_{True}$ . This answer cannot be granted in reality but for the sake of comparison we consider the true conductivity distribution is known in order to analyze the efficiency of the proposed optimization methods.

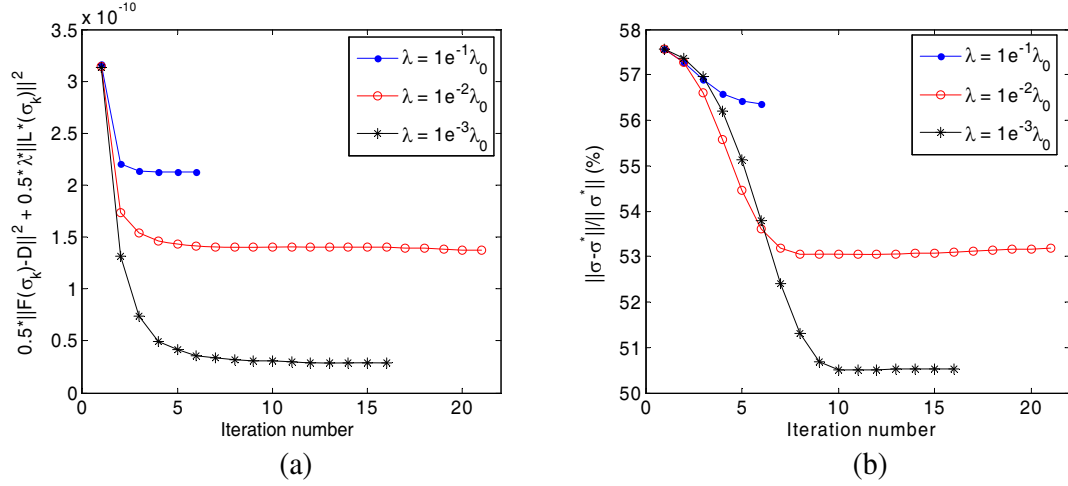


**Figure 5.** (a) Convergence plot of the objective function and (b) relative solution error versus iteration with Levenberg Marquardt method (simulated data from Ansys Maxwell).

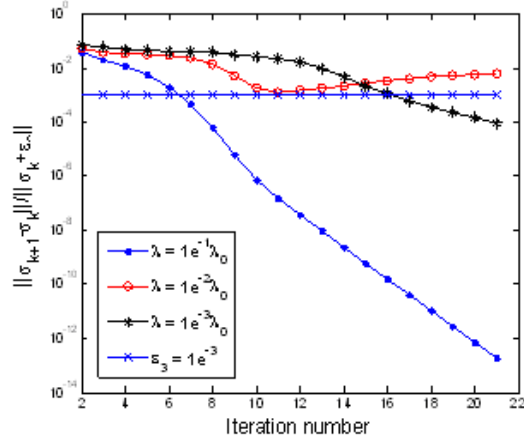


**Figure 6.** Performance of the stopping criterion for the LM method.

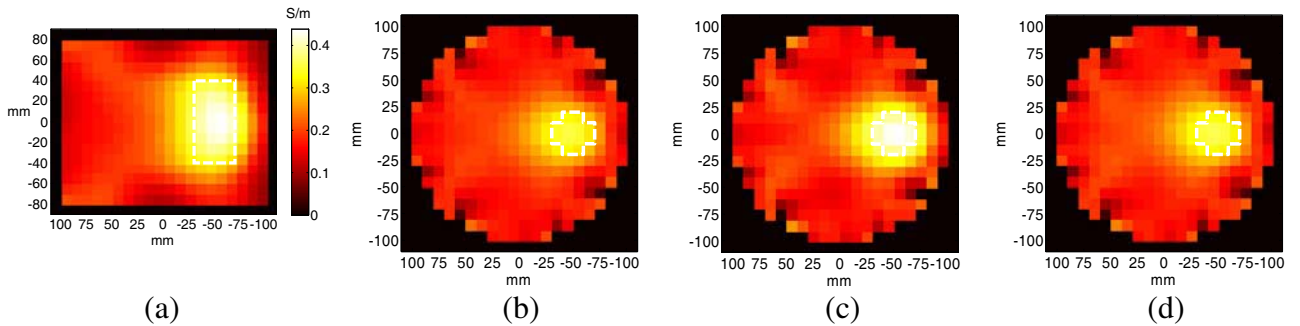


**Figure 7.** Reconstruction of conductivity distribution showing (a) vertical slice ( $x = 0$ ) mm, [(b); (c); (d)] horizontal slices in different  $z$  levels ( $z = -40$ ;  $z = 0$ ;  $z = 40$ ) mm, with Levenberg Marquardt method (simulated data from Ansys Maxwell;  $\lambda = 10^{-3}\lambda_0$ ).

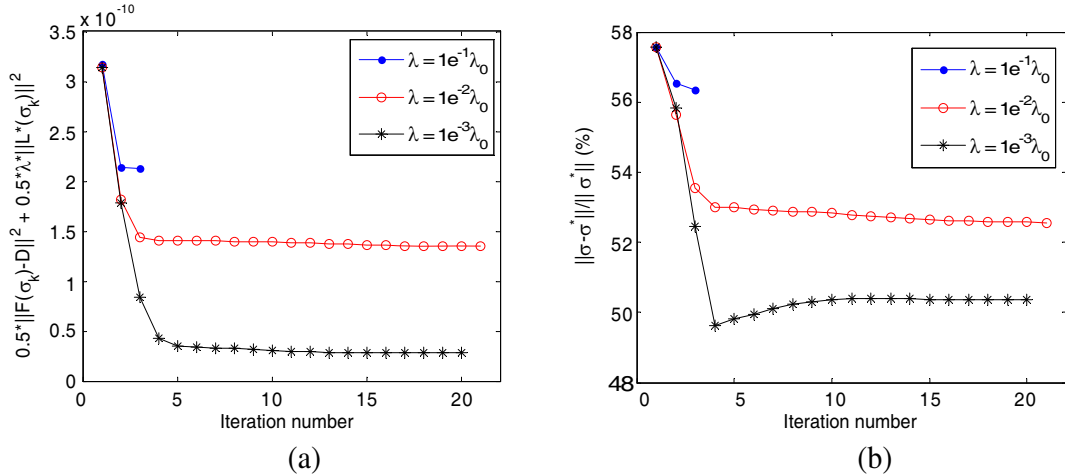


**Figure 8.** (a) Convergence plot of the objective function and (b) relative solution error versus iteration with Powell Dog Leg method (simulated data from Ansys Maxwell).

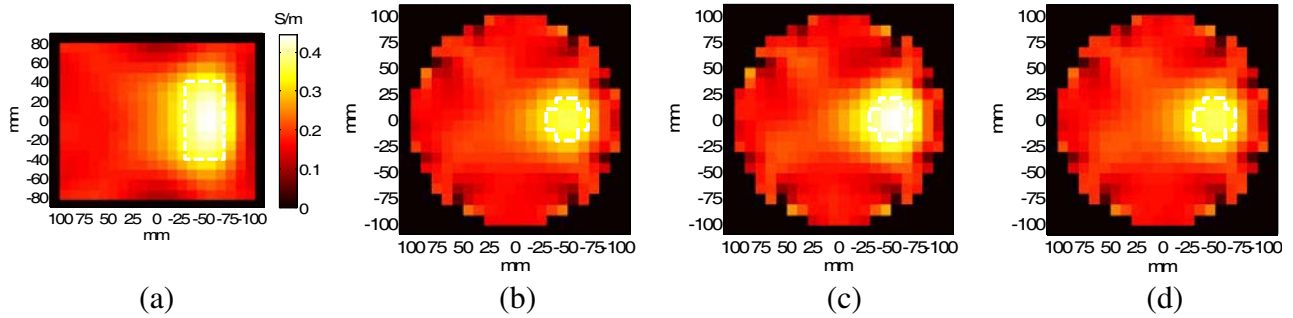


**Figure 9.** Reconstruction of conductivity distribution showing (a) vertical slice ( $x = 0$ ) mm, [(b); (c); (d)] horizontal slices in different  $z$  levels ( $z = -40$ ;  $z = 0$ ;  $z = 40$ ) mm, with Powell Dog Leg method (simulated data from Ansys Maxwell;  $\lambda = 10^{-3}\lambda_0$ ).

Figure 5(b) and Figure 8(b) depict the relative solution error norm over iteration using the LMM and the PDLM respectively. We observe that the LMM and PDLM produce similar solution error convergence levels for each value of  $\lambda$  with the smallest error achieved for  $\lambda = 1 \times 10^{-3}$  at just below 51%. More interestingly, the AGNM (Figure 10(b)) with its damping strategy applied to the regularisation parameter records the most superior solution error convergence with approximately 46%. This is reflected with a better quantitative convergence on the corresponding conductivity maps shown in Figure 11 compared with Figures 7 and 9. The reconstructed conductivity for the inclusion is approximately  $0.7 \text{ Sm}^{-1}$ , i.e.,  $\approx 155\%$  improvement compared to the LMM and the PDLM in which the inclusion conductivity is stagnated at about  $0.45 \text{ Sm}^{-1}$ . However, the reconstructed images (Figures 7 and 9) show that the LMM and the PDLM were able to preserve the smoothness of the background better than the AGNM in which some image artefacts are clearly noticeable. Another remark for all algorithms; there is a good correlation in the trends of the objective function convergence relative to the minimization of solution error at least for this reconstruction example, which provides confidence in the image reconstruction solution.

### 4.3. Stability of the Optimization

Stability of the image reconstruction algorithms is another important aspect. We can observe the LMM and the PDLM are able to provide better stability compared to the AGNM. These two methods provide better control by being able to switch between the Newton’s method and the steepest descent method.

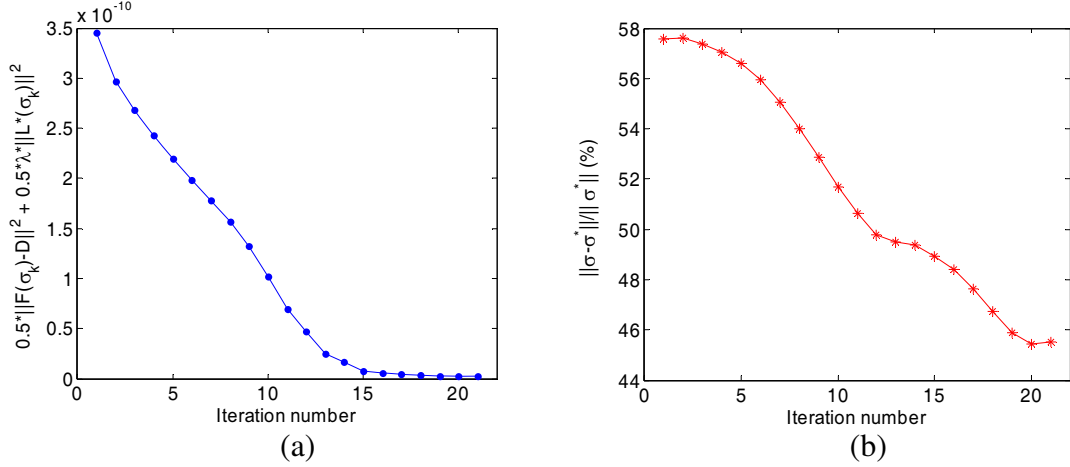


**Figure 10.** (a) Convergence plot of the objective function and (b) relative solution error versus iteration with Adaptive Gauss Newton method (simulated data from Ansys Maxwell).

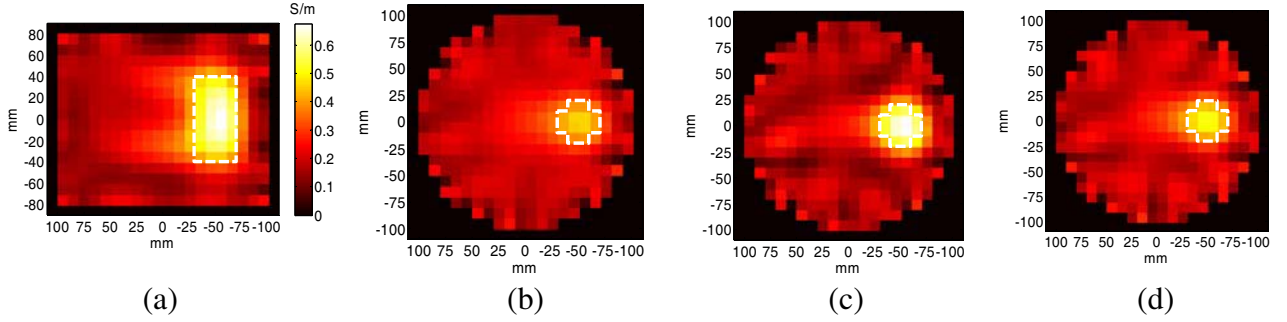


**Figure 11.** Reconstruction of conductivity distribution showing (a) vertical slice ( $x = 0$ ) mm, [(b); (c); (d)] horizontal slices in different  $z$  levels ( $z = -40$ ;  $z = 0$ ;  $z = 40$ ) mm, with Adaptive Gauss Newton method (simulated data from Ansys Maxwell).

Clearly we can see this effect in the final stage of the iteration where the LMM and the PDLM switch to small step sizes, which infer the steepest descent becomes dominant. This helps the image reconstruction to avoid unwanted divergence by enforcing the reconstruction algorithms to stay in the neighborhood of the local minimizer ( $\sigma^*$ ). Although the AGNM employs a similar damping process like the LMM, it is not a hybrid method and hence cannot benefit from the steepest descent method. However, the algorithm controls the stability by changing the regularization weight which seems to be a satisfactory approach.

#### 4.4. Robustness of the Stopping Criteria

The LMM and PDLM employ an endpoint strategy to their iterative procedure such that the iteration stops when the change in the conductivity solution i.e.,  $\delta\sigma_k$  is small. Since the LMM and PDLM eventually convert to using small steps for updating conductivity, this stopping strategy is theoretically adequate and reasonable. The performance of such stopping mechanism is illustrated in case of the LMM as shown in Figure 6. For the AGNM, this stopping criterion cannot be applied since the method is not guaranteed to switch to small step sizes toward the end of the iterative procedure. Hence, we are satisfied with the stopping technique that terminates the iteration when the descending condition for the objective function  $F$  is not met. However, the conductivity minimizer of the objective function in the AGNM cannot be guaranteed to be the minimizer of the solution error.

### 4.5. Sensitivity to the Choice of the Regularisation Parameter

For solving the MIT conductivity inverse problem, the LMM and PDLM require the specification of two parameters: the damping variable  $\gamma$  and the constant regularisation parameter  $\lambda$ . From the results we observed the methods are sensitive to the choice of such parameter, which infers a proper parameter selection method is required. However, the AGNM employs only one variable, i.e., the regularisation parameter which is involved in a damping process. The AGNM is not sensitive to the choice of initial value of the hyper-parameter  $\lambda_1$  as long it is sufficiently large to provide an initial smooth image, since it will then be reduced through the iterations. In this respect, the AGNM is better than the LMM and PDLM since it is less complex (employs less parameters) and is not sensitive to the choice of the regularisation parameter.

In order to assess the performance of absolute imaging as the MIT problem is scaled to higher resolutions, AGNM is selected for image reconstruction. Based on the above results, this nonlinear method is chosen due to its simplicity and adaptive approach in controlling the regularisation parameter. Otherwise, the other methods could have been employed for a similar purpose. Figure 12 shows the convergence of the objective function and the solution error norm for the image reconstruction of the head model (H1) using the AGNM-CG and AGNM methods. Clearly, similar degree of convergence is attained using both methods, which infers that there is no loss of accuracy caused by the application of the CG routine within the AGNM.

Figure 13 shows the cutaway plane displaying the reconstructed conductivity distribution using the AGNM-CG and AGNM methods. The reconstructed images clearly display the presence of the anomaly

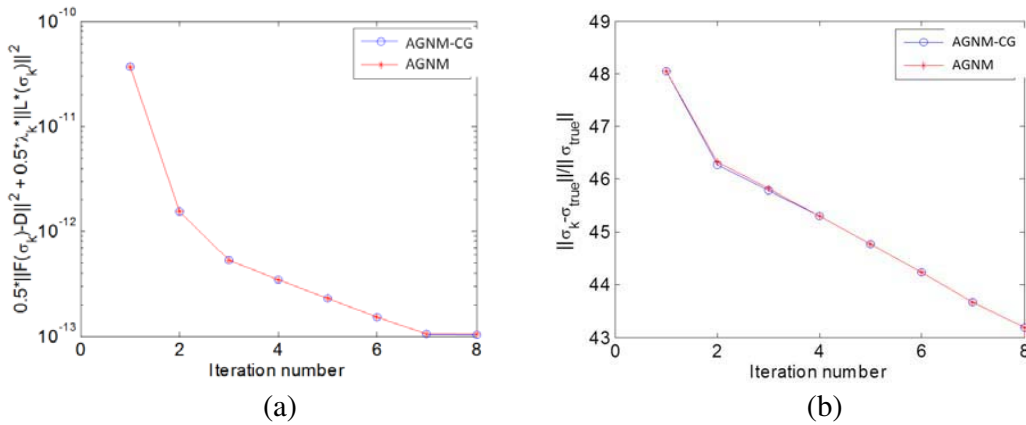


**Figure 12.** (a) Plot of the convergence of the objective function, and (b) the solution error norm.

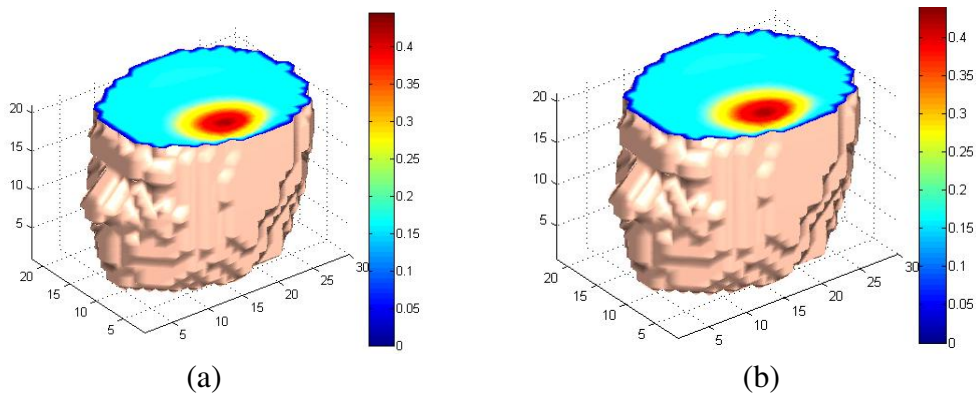


**Figure 13.** Reconstructed images for the medium large scale head model (H1), using (a) the AGNM-CG method and (b) the AGNM method.

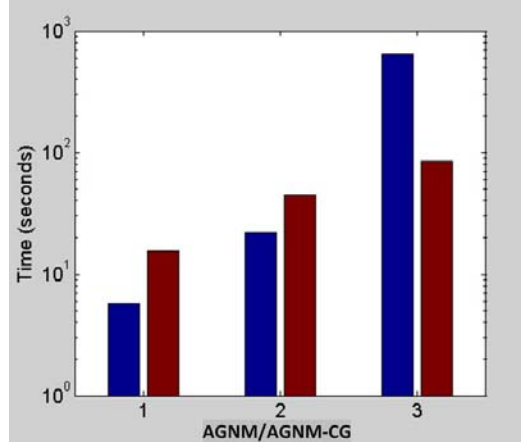


**Figure 14.** Average computation time per linearised step reconstruction for (1: example (P1); 2: head model (H1); 3 head model (H2)).

although with smoothing effect being noticeable. The two images resemble each other to a high extent which infers there is no loss in the image quality using the proposed CG method.

In order to assess the computational cost saving using the AGNM-CG method compared to the standard AGNM, the average time per iteration was calculated for the three problems with different resolutions. From Figure 14, it can be shown that as the problem size increases in scale, the computation time is reduced for the AGNM-CG. For the Head model with 30 k elements, the AGNM-CG is 8 times faster than the inversion based AGNM method.

## 5. CONCLUSIONS

The paper presented three image reconstruction algorithms for solving the MIT inverse problem for imaging low conductivity profiles. Using the damping and trust region techniques, the LMM and PDLM were illustrated to optimize the step in the iterative procedure. Likewise, the AGNM employed the damping technique to adapt the regularization parameter.

The results showed that the LMM and PDLM offered satisfactory stability especially toward the end of the optimization by converting to small step sizes calculated by the steepest descent method. Hence, we have provided evidence to indicate that these two methods can be useful to achieve a stable solution for reconstruction problems which can be useful for applications where data incorporates large errors. On the other hand, we have seen that AGNM provided finer convergence compared to its counterparts and required the specification of a lower number of parameters. Since this method does not employ the steepest descent method, it could be prone to unwanted divergence in the final stage of the iterations. For reconstruction problems with small noise characteristics, the method could provide better quantitative convergence with relatively higher resolution.

Using the AGNM method, reconstruction results with head phantom models showed the possibility of achieving the characterization of anomalies within highly meshed backgrounds. However, the reconstruction of such anomalies, especially in the cases where they are surrounded with complex material conductivity distributions may not yield similar reconstruction quality and may call for sophisticated regularization matrices such as structural regularization priors to be employed. The incorporation of the Krylov Subspace method, in this case the CG method within the AGNM algorithm, demonstrated the ability to overcome associated computational cost as the problem grows in scale.

## ACKNOWLEDGMENT

The authors would like to thank the UK Engineering and Physical Sciences Research Council (EPSRC) for their financial support under contract EP/E009158/1 (Imaging low-conductivity materials in Magnetic Induction Tomography — LCOMIT).

## REFERENCES

1. Griffiths, H., "Magnetic induction tomography," *Measurement Science & Technology*, Vol. 12, 1126–1131, 2001.
2. Peyton, A. J., Z. Z. Yu, G. Lyon, S. AlZeibak, J. Ferreira, J. Velez, F. Linhares, A. R. Borges, H. L. Xiong, N. H. Saunders, and M. S. Beck, "An overview of electromagnetic inductance tomography: Description of three different systems," *Measurement Science & Technology*, Vol. 7, 261–271, 1996.
3. Ke, L., X. Lin, and Q. Du, "An improved back-projection algorithm for magnetic induction tomography image reconstruction," *Advanced Materials Research*, Vol. 647, 630–635, 2013.
4. Korjenevsky, A., V. Cherepenin, and S. Sapetsky, "Magnetic induction tomography: Experimental realization," *Physiological Measurement*, Vol. 21, 89–94, 2000.
5. Merwa, R., K. Hollaus, P. Brunner, and H. Scharfetter, "Solution of the inverse problem of magnetic induction tomography (MIT)," *Physiological Measurement*, Vol. 26, S241–S250, 2005.
6. Scharfetter, H., K. Hollaus, J. Rosell-Ferrer, and R. Merwa, "Single-step 3-D image reconstruction in magnetic induction tomography: Theoretical limits of spatial resolution and contrast to noise ratio," *Annals of Biomedical Engineering*, Vol. 34, 1786–1798, 2006.
7. Scharfetter, H., P. Brunner, and R. Merwa, "Magnetic induction tomography: Single-step solution of the 3-D inverse problem for differential image reconstruction," *International Journal of Information and Systems Sciences*, Vol. 2, 585–606, 2006.
8. Vauhkonen, M., M. Hamsch, and C. H. Igney, "A measurement system and image reconstruction in magnetic induction tomography," *Physiological Measurement*, Vol. 29, S445–S454, 2008.
9. Ma, X., A. J. Peyton, S. R. Higson, A. Lyons, and S. J. Dickinson, "Hardware and software design for an electromagnetic induction tomography (EMT) system for high contrast metal process applications," *Measurement Science & Technology*, Vol. 17, 111–118, 2006.
10. Wei, H.-Y. and M. Soleimani, "Four dimensional reconstruction using magnetic induction tomography: Experimental study," *Progress In Electromagnetics Research*, Vol. 129, 17–32, 2012.
11. Wei, H.-Y. and M. Soleimani, "Volumetric magnetic induction tomography," *Measurement Science and Technology*, Vol. 23, No. 4, 055401, 2012.
12. Wei, H.-Y. and M. Soleimani, "Three-dimensional magnetic induction tomography imaging using a matrix free Krylov subspace inversion algorithm," *Progress In Electromagnetics Research*, Vol. 122, 29–45, 2012.
13. Watson, S., R. J. Williams, W. Gough, and H. Griffiths, "A magnetic induction tomography system for samples with conductivities below  $10 \text{ Sm}^{-1}$ ," *Measurement Science & Technology*, Vol. 19, No. 4, 11, 2008.
14. Soleimani, M. and W. R. B. Lionheart, "Absolute conductivity reconstruction in magnetic induction tomography using a nonlinear method," *IEEE Transactions on Medical Imaging*, Vol. 25, 1521–1530, 2006.
15. Soleimani, M., W. R. B. Lionheart, A. J. Peyton, X. D. Ma, and S. R. Higson, "A three-dimensional inverse finite-element method applied to experimental eddy-current imaging data," *IEEE Transactions on Magnetics*, Vol. 42, 1560–1567, 2006.
16. Hansen, P. C. and D. P. O'Leary, "The use of the L-curve in the regularization of discrete ill-posed systems," *SIAM J. Sci. Comput*, Vol. 14, No. 5, 1487–1503, 1993.
17. Goharian, M., M. Soleimani, and G. R. Moran, "A trust region subproblem for 3D electrical impedance tomography inverse problem using experimental data," *Progress In Electromagnetics Research*, Vol. 94, 19–32, 2009.
18. Goharian, M., A. Jegatheesan, and G. R. Moran, "Dogleg trust-region application in electrical impedance tomography," *Physiological Measurement*, Vol. 28, 555–572, 2007.
19. Tan, C., G. Xu, Y. Li, Y. Xuand, and G. Su, "Boundary image reconstruction based on the nonmonotonic and self-adaptive trust region method for electrical impedance tomography," *Physiological Measurement*, Vol. 34, 951–962, 2013.

20. Tan, C., Y. Xuand, and F. Dong, "Determining the boundary of inclusions with known conductivities using a Levenberg-Marquardt algorithm by electrical resistance tomography," *Measurement Science & Technology*, Vol. 22, 104005, 2011.
21. Kleefeld, A. and M. Reißel, "The Levenberg-Marquardt method applied to a parameter estimation problem arising from electrical resistivity tomography," *Applied Mathematics and Computation*, Vol. 217, 4490–4501, 2011.
22. Ren, S., F. Dong, Y. Xuand, and C. Tan "Reconstruction of the three-dimensional inclusion shapes using electrical capacitance tomography," *Measurement Science & Technology*, Vol. 25, 025403–025419, 2014.
23. Nielsen, H. B., "Damping parameter in Marquardt's method," Report IMM-REP-1999-05, Department of Mathematical Modelling, 31 pages, DTU, 1999.
24. Nocedal, J. and S. J. Wright, *Numerical Optimization*, Springer, ISBN 978-0-387-40065-5, 1999.
25. Frandsen, P. E., K. Jonasson, H. B. Nielsen, and O. Tingleff, *Unconstrained Optimization*, 3rd Edition, IMM, DTU, 2004.
26. Gazzola, S. and J. Nagy, "Generalized Arnoldi-Tikhonov method for sparse reconstruction," *SIAM J. Sci. Comput.*, Vol. 36, No. 2, B225–B247, 2014.
27. Biro, O. and K. Preis, "On the use of the magnetic vector potential in the Finite Element Analysis of 3 dimensional eddy currents," *IEEE Transactions on Magnetics*, Vol. 25, 3145–3159, 1989.
28. Hollaus, K., C. Magele, R. Merwa, and H. Scharfetter, "Numerical simulation of the eddy current problem in magnetic induction tomography for biomedical applications by edge elements," *IEEE Transactions on Magnetics*, Vol. 40, 623–626, 2004.
29. Morris, A., H. Griffiths, and W. Gough, "A numerical model for magnetic induction tomographic measurements in biological tissues," *Physiological Measurement*, Vol. 22, 113–119, 2001.
30. Pham, M. H. and A. J. Peyton, "A model for the forward problem in magnetic induction tomography using boundary integral equations," *IEEE Transactions on Magnetics*, Vol. 44, 2262–2267, 2008.
31. Dekdouk, B., W. Yin, C. Ktistis, D. W. Armitage, and A. J. Peyton, "A method to solve the forward problem in magnetic induction tomography based on the weakly coupled field approximation," *IEEE Trans. Biomed. Eng.*, Vol. 57, No. 4, 914–921, 2009.
32. Dyck, D. N., D. A. Lowther, and E. M. Freeman, "A method of computing the sensitivity of electromagnetic quantities to changes in materials and sources," *IEEE Transactions on Magnetics*, Vol. 30, 3415–3418, 1994.
33. Gabriel, S., R. W. Lau, and C. Gabriel, "The dielectric properties of biological tissues. 2 Measurements in the frequency range 10 Hz to 20 GHz," *Physics in Medicine and Biology*, Vol. 41, 2251–2269, 1996.
34. Madsen, K., H. B. Nielsen, and O. Tingleff, *Methods for Non-linear Least Squares Problems*, 2nd Edition, 2004.
35. Horesh, L., "Some novel approaches in modelling and image reconstruction for multi-frequency electrical impedance tomography of the human brain," PhD Thesis, 137–173, UCL, 2006.
36. Polydorides, N., W. R. B. Lionheart, and H. McCann, "Krylov subspace iterative techniques: On the detection of brain activity with electrical impedance tomography," *IEEE Transactions on Medical Imaging*, Vol. 21, 596–603, 2002.